Research Square

Preprints are preliminary reports that have not undergone peer review.
They should not be considered conclusive, used to inform clinical practice,
or referenced by the media as validated information.

A Bayesian Framework for Selecting Fractional Viscoelastic Models in Unconstrained-Layer Damped Beams

Lucas Asth

lucas.asth@iprj.uerj.br

Universidade do Estado do Rio de Janeiro

André Oliveira

Instituto Federal de Educação Ciência e Tecnologia do Norte de Minas Gerais

Diego Knupp

Universidade do Estado do Rio de Janeiro

Leonardo Stutz

Universidade do Estado do Rio de Janeiro

Arthur Adeodato

Universidade do Estado do Rio de Janeiro

Research Article

Keywords: Fractional viscoelasticity, Free layer damping, Model selection, Global sensitivity analysis, Bayesian inference

Posted Date: November 5th, 2026

DOI: https://doi.org/10.21203/rs.3.rs-11455292/v1

License: This work is licensed under a Creative Commons Attribution 4.0 International License.
Read Full License

Additional Declarations: No competing interests reported.

A Bayesian Framework for Selecting Fractional Viscoelastic Models in Unconstrained-Layer Damped Beams

Lucas S. Asth*[1], André J. P. de Oliveira[1, 2], Diego C. Knupp[1], Leonardo T. Stutz[1], and Arthur Adeodato[1]

[1]*Polytechnic Institute, Rio de Janeiro State University, IPRJ/UERJ, Rua Bonfim 25, Vila Amélia, Nova Friburgo, RJ, 28625-570, Brazil.*
[2]*Federal Institute of Northern Minas Gerais, IFNMG, Campus Porteirinha, Avenida José Silveira Lopes, nº 429 Vila Serranópolis, Porteirinha - MG, 39520-000, Brazil.*

Abstract

This work presents a Bayesian framework for the identification and selection of fractional viscoelastic constitutive models for layered beams with unconstrained damping treatments. The physical problem is described by one-dimensional homogenized beam models, in which the viscoelastic layer is represented through a frequency-dependent complex modulus. Both the classical thin-layer formulation and a shear-corrected thick-layer model are considered through a unified effective flexural stiffness. The resulting frequency-domain boundary value problem is solved by the Generalized Integral Transform Technique (GITT), leading to a semi-analytical expression for the beam-tip receptance. This formulation provides an efficient forward model for repeated evaluations in inverse analysis. Several fractional viscoelastic models, including Kelvin–Voigt, Maxwell and Zener formulations, are investigated as competing model classes. Bayesian parameter estimation is performed using Transitional Markov Chain Monte Carlo (TMCMC), which provides posterior samples of the constitutive parameters and estimates of the model evidence. The evidence is then used for Bayesian model class selection, naturally balancing data-fitting capability and model complexity. In addition, global sensitivity analysis is employed to assess the influence and practical identifiability of the uncertain parameters on the frequency-response predictions. The proposed methodology combines a mesh-free semi-analytical structural solver with a probabilistic framework for uncertainty quantification, parameter estimation, and model comparison. The results demonstrate that the GITT-based forward model is suitable for Bayesian inverse analysis of viscoelastic layered beams, enabling the systematic evaluation of competing fractional constitutive descriptions from frequency-response data. The model comparison shows that layer thickness determines which constitutive model is favored by the data, suggesting geometry as an integral part of constitutive-model identifiability.

Keywords: Fractional viscoelasticity, Free layer damping, Model selection, Global sensitivity analysis, Bayesian inference.

*Corresponding author: lucas.asth@iprj.uerj.br

1 Introduction

Lightweight mechanical and structural systems often exhibit low inherent damping and may therefore become susceptible to excessive vibration, noise, and fatigue under dynamic loading. Passive viscoelastic treatments provide an attractive means of increasing energy dissipation because they are relatively simple to implement, require no external power supply, and can operate over broad frequency ranges [1, 2]. Among the available configurations, constrained- and unconstrained-layer treatments have been extensively used to introduce damping into host structures [3–6]. Although constrained-layer damping generally provides greater energy dissipation through shear deformation of the viscoelastic core, unconstrained or free-layer treatments remain particularly appealing because of their simpler construction, reduced structural complexity, and direct applicability to beam-like components.

The reliable prediction of the dynamic response of beams treated with unconstrained viscoelastic layers involves two closely related challenges: the mechanical representation of the layered structure and the constitutive description of the damping material. From a structural-modeling perspective, classical homogenized Euler–Bernoulli formulations are generally adequate when the viscoelastic layer is sufficiently thin and transverse shear deformation is negligible [7, 8]. As the layer thickness increases, however, shear deformation may significantly modify resonance frequencies, response amplitudes, and the overall frequency-response pattern. Consequently, a formulation developed for thin damping layers cannot be assumed to remain accurate for thicker treatments, for which shear-corrected homogenized models provide a more consistent mechanical description [7–9].

The second challenge arises from the intrinsic frequency dependence of viscoelastic materials. Their storage modulus, loss modulus, and loss factor may vary substantially with frequency and temperature, and this behavior must be incorporated into the structural model to obtain reliable frequency-response predictions [5, 6]. Several constitutive frameworks have been proposed for this purpose, including complex-modulus, Golla–Hughes–McTavish, anelastic displacement field, and fractional-derivative representations [6, 10–12]. Fractional viscoelastic models are particularly attractive because they can describe hereditary effects and power-law-type relaxation behavior using a relatively small number of parameters [13–16]. In the frequency domain, fractional derivatives are mapped into complex powers of the excitation frequency, allowing the material memory to be incorporated directly into the complex modulus. This property makes fractional models especially convenient for vibration analysis based on measured or simulated frequency-response functions [5, 17–19].

The identification of viscoelastic constitutive parameters from vibration data has consequently received considerable attention. Conventional procedures include dynamic mechanical analysis, Oberst-type beam tests, and inverse approaches in which measured modal properties or frequency-response functions are matched by numerical predictions. Kim and Lee [5], for example, identified the parameters of a fractional derivative model from measured FRFs of an unconstrained-layer damped beam, demonstrating the benefit of using information distributed over a frequency interval rather than relying only on isolated resonance frequencies. Sun et

al. [6] developed an inverse procedure for identifying the frequency-dependent properties of a viscoelastic core from vibration-response data. Other studies have addressed the inverse characterization of viscoelastic layers in beams, plates, and sandwich structures using optimization-based strategies [17, 20]. Although these contributions demonstrate the practical relevance of FRF-based identification, the constitutive law is generally selected beforehand, and the inverse problem is restricted to estimating the parameters of that prescribed model.

This limitation is relevant because different fractional constitutive models may produce similar frequency-response curves after calibration while implying different asymptotic behavior, parameter correlations, physical interpretations, and extrapolation capabilities. Deterministic goodness-of-fit criteria alone may therefore be insufficient for selecting a constitutive law. Bayesian model class selection provides a statistically consistent alternative through the model evidence, or marginal likelihood, which averages the likelihood over the prior parameter domain and naturally balances data-fitting capability against effective model complexity [21–23].

Bayesian inference is also well suited to the identification of viscoelastic properties because it represents the uncertain constitutive parameters through posterior probability distributions rather than isolated deterministic estimates [24, 25]. This is particularly relevant for nonlinear inverse problems in which measurement noise, weak parameter influence, and compensating parameter effects may produce correlated or weakly identifiable solutions. In the present work, Transitional Markov Chain Monte Carlo (TMCMC) is adopted because it provides posterior samples and an estimate of the model evidence within the same sequential sampling procedure, thereby enabling parameter estimation and model class comparison within a unified probabilistic framework [26–28].

Eigenfunction-based semi-analytical formulations are attractive in this context because they avoid repeated spatial discretization and large-scale matrix assembly while preserving the essential structure of the governing problem. The Generalized Integral Transform Technique (GITT) provides a hybrid analytical–numerical framework in which the spatial dependence of the response is represented through eigenfunction expansions, reducing the boundary-value problem to transformed equations or compact series expressions [29–31]. In the present frequency-domain formulation, the effective complex flexural stiffness incorporates the constitutive behavior directly into the transformed equations, yielding a unified representation that accommodates different fractional viscoelastic model classes.

A complementary issue concerns how the available FRF data inform the parameters of each competing constitutive model. Variance-based global sensitivity analysis provides a systematic means of quantifying parameter influence over the complete prior domain and of separating direct effects from interaction effects [32, 33].

An additional unresolved question is whether the constitutive representation favored by the data remains unchanged when the mechanical configuration of the layered beam is modified. Even when the same viscoelastic material is considered, thin- and thick-layer configurations transmit its frequency-dependent behavior differently to the global structural response because transverse shear becomes increasingly relevant as the damping-layer thickness increases. The adopted me-

chanical formulation may therefore affect not only parameter sensitivity and practical identifiability, but also the relative plausibility of competing constitutive classes.

In this work, a Bayesian framework is developed for parameter identification and model class selection in cantilever beams with unconstrained viscoelastic-layer damping. The structural response is described through a unified frequency-domain formulation encompassing the classical thin-layer model and a shear-corrected thick-layer model, and the resulting boundary-value problem is solved using the GITT. Synthetic FRF observations are generated with a finite-element reference model employing a four-parameter fractional law, whose parameter values were obtained from a fit to real experimental data reported in [7, 34]. The candidate set comprises the fractional Kelvin–Voigt, Maxwell, and Zener models. Using the finite-element model for data generation and the GITT formulation for the candidate predictions mitigates the inverse crime and introduces a numerical-model mismatch. For each candidate class, TMCMC is used to estimate the posterior distribution of the constitutive parameters and the corresponding Bayesian evidence, from which the posterior model probabilities are determined. Likelihood-based Sobol indices support the interpretation of parameter influence and interaction effects.

The main contributions of the study are threefold. First, a unified thin/thick-layer formulation is combined with an eigenfunction-based semi-analytical GITT solution, providing an efficient forward model for repeated frequency-response evaluations. Second, competing fractional constitutive laws are compared through Bayesian evidence rather than through deterministic calibration alone, thereby accounting simultaneously for predictive agreement, parameter uncertainty, and effective model complexity. Third, the study investigates how shear-related effects modify the likelihood structure, the information conveyed by the FRF data, and the constitutive class favored by Bayesian model selection.

The remainder of this paper is organized as follows. Section 2 presents the frequency-domain formulation of the homogenized thin- and thick-layer beam models and the corresponding semi-analytical solution obtained using the Generalized Integral Transform Technique (GITT). Section 3 introduces the candidate fractional viscoelastic constitutive models and describes the Bayesian framework for parameter identification and model class selection based on TMCMC. Section 4 presents and discusses the numerical results, including verification of the GITT formulation, global sensitivity analysis, posterior parameter estimation, and Bayesian model comparison for both layer configurations. Finally, Section 5 summarizes the main findings and discusses the limitations and potential extensions of the proposed framework.

2 Frequency-domain formulation and hybrid GITT solution

Consider a uniform cantilever beam composed of an elastic base layer and an unconstrained viscoelastic layer, with thicknesses H and H_1, respectively, and common width b. Figure 1 shows a schematic representation of the model.

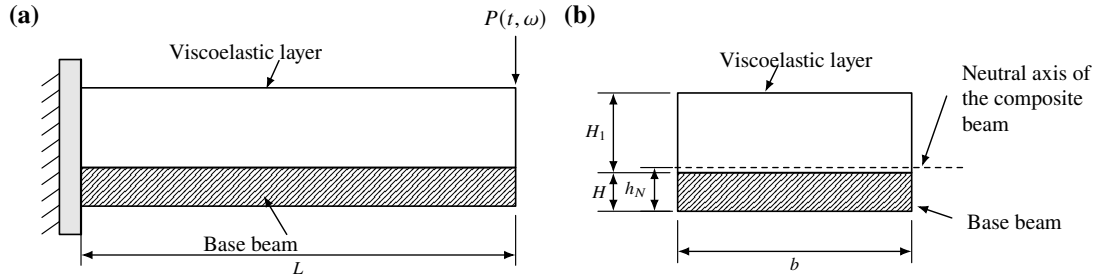


Figure 1: Schematic representation of the unconstrained viscoelastic-layer beam: (a) cantilever configuration subjected to a harmonic transverse force $P(\omega)$ at the free end; and (b) cross-section of the two-layer composite beam, indicating the base and viscoelastic layers, their respective thicknesses, the beam width, and the position of the neutral axis.

The mass per unit length and the shear moduli are

$$m_L = b\left(\rho H + \rho_1 H_1\right), \qquad G = \frac{E}{2(1+\nu)}, \qquad G_v^*(\omega) = \frac{E_v^*(\omega)}{2(1+\nu_1)}, \tag{1}$$

where $E_v^*(\omega)$ is the frequency-dependent complex modulus of the viscoelastic material.

The homogenized flexural stiffness proposed by Cortés and Elejabarrieta [7] is adopted directly. For the classical thin-layer model, in which transverse shear deformation is neglected, the equivalent complex stiffness is

$$B_{eq}(\omega) = EI_b(\omega) + E_v^*(\omega) I_v(\omega), \tag{2}$$

where

$$h_N(\omega) = \frac{EH^2 + E_v^*(\omega) H_1 (2H + H_1)}{2\left[EH + E_v^*(\omega) H_1\right]}, \tag{3}$$

$$I_b(\omega) = \frac{bH^3}{12} + bH\left[h_N(\omega) - \frac{H}{2}\right]^2, \qquad I_v(\omega) = \frac{bH_1^3}{12} + bH_1\left[H + \frac{H_1}{2} - h_N(\omega)\right]^2. \tag{4}$$

In Eq. (4), $I_b(\omega)$, and $I_v(\omega)$ represent the moments of inertia of the base and viscoelastic layer, respectively. Because the neutral-axis position depends on $E_v^*(\omega)$, the quantities $h_N(\omega)$, $I_b(\omega)$, and $I_v(\omega)$ are generally complex and should be interpreted as section-equivalent quantities introduced by the homogenization procedure, rather than as purely geometric properties [7].

For each fixed excitation frequency, they are constant complex coefficients that account for the frequency-dependent stiffness and phase lag of the viscoelastic layer. In the subsequent thick-layer formulation, these quantities are used to define the dimensionless sectional parameters $r_N(\omega)$ and $r_I(\omega)$, which enter the equivalent shear-stiffness expressions and, ultimately, the shear-corrected flexural stiffness $B_K(\omega)$.

For thick viscoelastic layers, transverse shear is incorporated through the equivalent shear stiffness derived in Ref. [7],

$$\frac{1}{K_{eq}(\omega)} = \frac{1}{K_b(\omega)} + \frac{1}{K_v(\omega)}. \tag{5}$$

For compactness, the following dimensionless quantities are introduced:

$$M(\omega) = \frac{E_v^*(\omega)}{E}, \qquad T = \frac{H_1}{H}, \qquad r_N(\omega) = \frac{2h_N(\omega)}{H}, \qquad r_I(\omega) = \frac{I_v(\omega)}{I_b(\omega)}, \tag{6}$$

together with

$$D(\omega) = \left[1 + r_I(\omega)M(\omega)\right]^2 \left\{1 + 3\left[r_N(\omega) - 1\right]^2\right\}^2. \tag{7}$$

The shear-flexibility contributions of the elastic and viscoelastic layers are then given by [7]

$$\frac{1}{K_b(\omega)} = \frac{6}{5GbH}\frac{10r_N^2 - 15r_N + 6}{D(\omega)}, \tag{8}$$

and

$$\frac{1}{K_v(\omega)} = \frac{6}{5G_v^*(\omega)bH_1}\frac{M^2T^4\left(10r_N^2 - 40r_N - 25r_NT + 16T^2 + 50T + 40\right)}{D(\omega)}, \tag{9}$$

where the frequency arguments of M and r_N have been omitted in Eq. (9) for conciseness.

The corresponding shear-corrected flexural stiffness is [7]

$$B_K(\omega) = \frac{B_{eq}(\omega)}{\left[\sqrt{1 + \psi^2(\omega)} + \psi(\omega)\right]^2}, \tag{10}$$

with

$$\psi(\omega) = \frac{\omega\sqrt{m_L B_{eq}(\omega)}}{2K_{eq}(\omega)}. \tag{11}$$

The square roots in Eqs. (10) and (11) are evaluated continuously from the static limit. The thin- and thick-layer models can therefore be represented by the unified stiffness

$$B_{\text{eff}}(\omega) = \begin{cases} B_{eq}(\omega), & \text{thin-layer formulation,} \\ B_K(\omega), & \text{shear-corrected thick-layer formulation.} \end{cases} \tag{12}$$

Following the harmonic representation

$$w(x,t) = \Re\left\{\hat{w}(x,\omega)e^{i\omega t}\right\}, \qquad P(t) = \Re\left\{\hat{P}(\omega)e^{i\omega t}\right\}, \tag{13}$$

For each excitation frequency, the complex displacement amplitude satisfies

$$B_{\text{eff}}(\omega)\frac{d^4\hat{w}(x,\omega)}{dx^4} - m_L\omega^2\hat{w}(x,\omega) = 0, \qquad 0 < x < L, \tag{14}$$

with clamped and harmonically loaded free-end conditions, respectively,

$$\hat{w}(0,\omega) = \hat{w}'(0,\omega) = 0, \tag{15a}$$

$$\hat{w}''(L,\omega) = 0, \qquad -B_{\text{eff}}(\omega)\hat{w}'''(L,\omega) = \hat{P}(\omega). \tag{15b}$$

The boundary-value problem is solved using the Transform Technique [30, 35]. The transformation basis is obtained from the classical homogeneous cantilever eigenvalue problem

$$\phi_i^{(4)}(x) - \beta_i^4\phi_i(x) = 0, \qquad 0 < x < L, \tag{16a}$$

$$\phi_i(0) = \phi_i'(0) = 0, \qquad \phi_i''(L) = \phi_i'''(L) = 0, \tag{16b}$$

$$\beta_i = \frac{\lambda_i}{L}, \qquad \cosh(\lambda_i)\cos(\lambda_i) + 1 = 0. \tag{16c}$$

A convenient unnormalized form of the classical cantilever eigenfunctions associated with the positive roots λ_i is [36, 37]

$$\begin{aligned} \phi_i(x) &= \cosh(\beta_i x) - \cos(\beta_i x) - \sigma_i\left[\sinh(\beta_i x) - \sin(\beta_i x)\right], \\ \sigma_i &= \frac{\cosh(\lambda_i) + \cos(\lambda_i)}{\sinh(\lambda_i) + \sin(\lambda_i)}, \qquad i = 1, 2, 3, \ldots. \end{aligned} \tag{17}$$

For use in the integral transform pair, these eigenfunctions are normalized with respect to the mass per unit length m_L according to

$$N_i = \int_0^L m_L \phi_i^2(x)\, dx, \tag{18a}$$

$$\tilde{\phi}_i(x) = \frac{\phi_i(x)}{\sqrt{N_i}}, \tag{18b}$$

$$\int_0^L m_L \tilde{\phi}_i(x)\tilde{\phi}_j(x)\, dx = \delta_{ij}. \tag{18c}$$

the direct and inverse transform pair is written as [30, 35, 38]

$$\eta_i(\omega) = \int_0^L m_L \tilde{\phi}_i(x)\hat{w}(x,\omega)\, dx, \tag{19a}$$

$$\hat{w}(x,\omega) = \sum_{i=1}^{\infty} \tilde{\phi}_i(x)\eta_i(\omega), \tag{19b}$$

where $\eta_i(\omega)$ is the transformed modal amplitude. Projecting Eq. (14) onto $\tilde{\phi}_i(x)$ and integrating the fourth-order term by parts yields the uncoupled algebraic problem

$$\left[\frac{B_{\text{eff}}(\omega)}{m_L}\beta_i^4 - \omega^2\right]\eta_i(\omega) = \hat{P}(\omega)\tilde{\phi}_i(L), \tag{20a}$$

$$\eta_i(\omega) = \frac{\hat{P}(\omega)\tilde{\phi}_i(L)}{\dfrac{B_{\text{eff}}(\omega)}{m_L}\beta_i^4 - \omega^2}. \tag{20b}$$

The tip-force contribution in Eq. (20a) results from the nonhomogeneous shear boundary condition in Eq. (15b); all other boundary terms vanish because the physical and auxiliary problems satisfy compatible homogeneous conditions. Thus, the frequency dependence and viscoelastic dissipation are contained entirely in $B_{\text{eff}}(\omega)$, whereas the spatial eigenfunctions are independent of ω.

For numerical evaluation, the inverse expansion is truncated after N modes,

$$\hat{w}^{(N)}(x,\omega) = \sum_{i=1}^{N} \tilde{\phi}_i(x)\eta_i(\omega). \tag{21}$$

The receptance between the force applied at $x = L$ and the displacement at an arbitrary position x is consequently

$$H^{(N)}(x,\omega) = \frac{\hat{w}^{(N)}(x,\omega)}{\hat{P}(\omega)} = \sum_{i=1}^{N} \frac{\tilde{\phi}_i(L)\tilde{\phi}_i(x)}{\dfrac{B_{\text{eff}}(\omega)}{m_L}\beta_i^4 - \omega^2}. \tag{22}$$

In the present study, the frequency-response function is evaluated at the free end by setting $x = L$ in Eq. (22). The truncation order N is increased until the response becomes insensitive to the inclusion of additional modes over the frequency range of interest.

3 Candidate fractional viscoelastic constitutive models

The frequency-domain beam formulation developed in Section 2 depends on the constitutive behavior of the viscoelastic layer only through its complex modulus $E_v^*(\omega)$. For a harmonic steady-state response,

$$E_v^*(\omega) = \frac{\hat{\sigma}(\omega)}{\hat{\varepsilon}(\omega)}, \qquad \mathcal{F}\{D_t^\alpha f(t)\} = (i\omega)^\alpha \hat{f}(\omega), \tag{23}$$

where $0 < \alpha < 1$. For positive frequencies, the principal branch

$$(i\omega)^\alpha = \omega^\alpha \left[\cos\Big(\frac{\pi\alpha}{2}\Big) + i\sin\Big(\frac{\pi\alpha}{2}\Big)\right] \tag{24}$$

is adopted. The frequency-domain expressions employed below follow directly from the classical fractional constitutive equations [13–16].

The reference constitutive law adopted in the present study is the fractional standard linear solid model employed in [7]. The corresponding parameter values were obtained by fitting this model to real experimental data reported in [34]. This same constitutive law is used to generate the synthetic reference observations employed in the inverse analysis. Specifically, the reference frequency-response vector is computed with the finite-element model using the experimentally calibrated parameter vector: $\boldsymbol{\theta}_{\text{ref}} = [E_{0,\text{ref}}, E_{\infty,\text{ref}}, \tau_{\text{ref}}, \alpha_{\text{ref}}]^\top$.

The competing constitutive classes are the fractional Kelvin–Voigt, Maxwell, and Zener models, $\mathcal{M} = \{\mathcal{M}_{\text{KV}}, \mathcal{M}_{\text{M}}, \mathcal{M}_{\text{Z}}\}$.

The corresponding complex moduli supplied to the structural forward model are

$$E_{\text{KV}}^*(\omega) = E_v + \eta(i\omega)^\alpha, \tag{25a}$$

$$E_{\text{M}}^*(\omega) = \frac{E_v\eta(i\omega)^\alpha}{E_v + \eta(i\omega)^\alpha}, \tag{25b}$$

$$E_{\text{Z}}^*(\omega) = \frac{E_0 + E_\infty(i\tau\omega)^\alpha}{1 + (i\tau\omega)^\alpha}. \tag{25c}$$

In the fractional Kelvin–Voigt and Maxwell models, E_v is the spring modulus and η is the fractional viscoelastic coefficient. In the fractional Zener model, E_0 and E_∞ are the relaxed and unrelaxed moduli, corresponding to the low- and high-frequency limits, respectively, and τ is the characteristic relaxation time, with $0 < E_0 < E_\infty$. The corresponding uncertain parameter vectors and limiting moduli are summarized in Table 1 and their rheological arrangements are illustrated in Fig. 2

Table 1: Parameterizations and limiting moduli of the candidate fractional viscoelastic models.

Model	**Parameter vector**	$E^*(0)$	$E^*(\infty)$
Fractional Kelvin–Voigt	$[E_v, \eta, \alpha]^\top$	E_v	Unbounded
Fractional Maxwell	$[E_v, \eta, \alpha]^\top$	0	E_v
Fractional Zener	$[E_0, E_\infty, \tau, \alpha]^\top$	E_0	E_∞

The limits reported in Table 1 describe the relaxed, or long-time, behavior as $\omega \to 0$ and the unrelaxed, or short-time, behavior as $\omega \to \infty$. The Kelvin–Voigt model retains the equilibrium stiffness E_v at low frequencies, whereas its modulus becomes unbounded because the fractional contribution grows as ω^α. Conversely, the Maxwell model has no equilibrium stiffness and approaches E_v at high frequencies. The Zener model remains bounded between E_0 and E_∞, thereby representing a transition between finite relaxed and unrelaxed stiffnesses. These distinct limiting behaviors provide the main constitutive differences to be assessed through Bayesian model class selection.

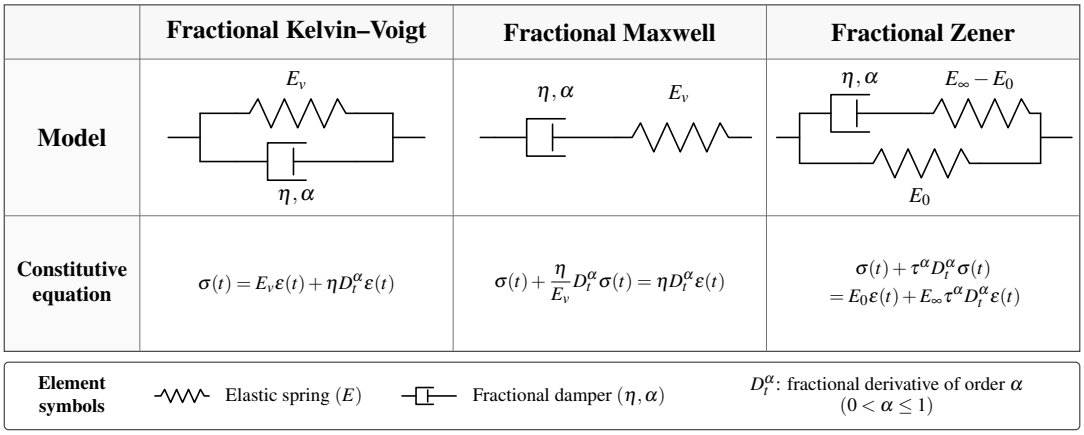


Figure 2: Rheological representations and time-dependent stress–strain relations of the fractional Kelvin–Voigt, Maxwell, and Zener constitutive models.

The equations displayed in Fig. 2 are the time-domain constitutive relations connecting stress and strain for each rheological arrangement. Under the harmonic assumption, applying the fractional Fourier mapping in Eq. (23) replaces each fractional derivative by the factor $(i\omega)^\alpha$. Solving the transformed constitutive equation for the ratio $\hat{\sigma}(\omega)/\hat{\varepsilon}(\omega)$ then gives the complex moduli in Eqs. (25).

Accordingly, the Zener expression in Eq. (25c) corresponds to the four-parameter fractional standard linear solid adopted in the reference studies [7, 34].

The fractional Zener model is retained among the candidate classes to provide a controlled benchmark for evaluating the ability of the Bayesian framework to recover the data-generating constitutive law and its parameters. Its inclusion does not make the model-selection problem trivial, since the synthetic observations contain noise and are generated using a finite-element model, whereas the candidate responses are computed using the GITT formulation. Moreover, Bayesian evidence accounts not only for the best achievable fit but also for parameter uncertainty and effective model complexity. Consequently, the Zener model is favored only if the available frequency-response data contain sufficient information to support its additional constitutive flexibility over the simpler Kelvin–Voigt and Maxwell alternatives.

The elastic moduli E_v, E_0, and E_∞ have units of pressure. The fractional coefficient η, used in the Kelvin–Voigt and Maxwell models, has units $[\eta] = \mathrm{Pa\,s}^\alpha$, whereas the Zener relaxation time τ has units of time and α is dimensionless. For each candidate model and sampled parameter vector, the corresponding expression in Eqs. (25) is evaluated at the prescribed excitation frequencies and substituted into the homogenized formulation of Section 2. The resulting $B_{eq}(\omega)$, $K_{eq}(\omega)$, and $B_{\mathrm{eff}}(\omega)$ are then introduced into the GITT receptance. Thus, the structural solver remains unchanged across the candidate classes; only the constitutive expression for $E_v^*(\omega)$ and its associated parameter vector are modified.

3.1 Bayesian inference

Bayesian inference provides a probabilistic framework for updating uncertain model parameters by combining prior information with observed data, while consistently quantifying the associated uncertainty [39, 40]. Let $\mathcal{M}$ denote the set of candidate constitutive model classes,

$$\boldsymbol{\mathcal{M}} = \{\mathcal{M}_1, \ldots, \mathcal{M}_{N_m}\}, \tag{26}$$

where N_m is the number of candidate classes. In the present analysis, these classes correspond to the fractional Kelvin–Voigt, Maxwell, and Zener models. For a given class $\mathcal{M}_j$, the uncertain parameter vector $\boldsymbol{\theta} \in \Theta_j$ is treated as a random variable, and the objective is to infer its joint posterior probability density $p(\boldsymbol{\theta} \mid \boldsymbol{\mathcal{D}}, \mathcal{M}_j)$.

In the present study, $\boldsymbol{\mathcal{D}}$ is generated synthetically by adding a prescribed random observation error to the frequency-response vector produced by the finite-element reference model. Accordingly, $\boldsymbol{\mathcal{D}}$ is regarded as one realization of a random observation vector defined at the sampled frequencies. For each candidate class, $\boldsymbol{A}(\boldsymbol{\theta} \mid \mathcal{M}_j)$ denotes the corresponding vector of response amplitudes predicted by the GITT-based forward formulation. The reference parameters and noise level used to generate the observations are reported in Section 4. The assumptions adopted in the inverse analysis are summarized in Table 2.

Table 2: Statistical and modeling assumptions adopted in the Bayesian inverse analysis.

No.	Assumption
1	The parameter vector $\boldsymbol{\theta}$ is constant over the frequency range considered in the inverse analysis.
2	The prior probability density $p(\boldsymbol{\theta} \mid \mathcal{M}_j)$ is prescribed for each candidate model class.
3	The geometry, boundary conditions, excitation, frequency grid, and all physical properties not included in $\boldsymbol{\theta}$ are treated as known deterministic quantities.
4	For a prescribed parameter vector, the predicted response $\boldsymbol{A}(\boldsymbol{\theta} \mid \mathcal{M}_j)$ is deterministic, and no separate stochastic model-discrepancy term is introduced.
5	The synthetic data vector $\boldsymbol{\mathcal{D}}$ is treated as one realization of a random observation vector defined at the sampled frequencies.
6	The observation errors are additive zero-mean Gaussian random variables with prescribed covariance matrix $\mathbf{W}$.
7	The observation errors are statistically independent of the uncertain parameters.
8	The same observations and error model are used for all candidate classes, which are assigned equal prior probabilities.

According to Bayes' theorem [24], the posterior probability density for model class $\mathcal{M}_j$ is

$$p(\boldsymbol{\theta} \mid \boldsymbol{\mathcal{D}}, \mathcal{M}_j) = \frac{p(\boldsymbol{\theta} \mid \mathcal{M}_j) p(\boldsymbol{\mathcal{D}} \mid \boldsymbol{\theta}, \mathcal{M}_j)}{p(\boldsymbol{\mathcal{D}} \mid \mathcal{M}_j)}. \tag{27}$$

Here, $p(\boldsymbol{\theta} \mid \mathcal{M}_j)$ is the prior probability density, $p(\boldsymbol{\mathcal{D}} \mid \boldsymbol{\theta}, \mathcal{M}_j)$ is the likelihood function, and $p(\boldsymbol{\mathcal{D}} \mid \mathcal{M}_j)$ is the marginal likelihood, also called the model evidence, defined as

$$p(\boldsymbol{\mathcal{D}} \mid \mathcal{M}_j) = \int_{\Theta_j} p(\boldsymbol{\theta} \mid \mathcal{M}_j) p(\boldsymbol{\mathcal{D}} \mid \boldsymbol{\theta}, \mathcal{M}_j) \, \mathrm{d}\boldsymbol{\theta}, \tag{28}$$

where Θ_j is the admissible parameter domain for $\mathcal{M}_j$. Considering the residual between the observed amplitudes and the corresponding model predictions as additive, independent of $\boldsymbol{\theta}$, and Gaussian distributed with zero mean and covariance matrix $\mathbf{W}$, the likelihood function is given by [24]

$$p(\boldsymbol{\mathcal{D}} | \boldsymbol{\theta}, \mathcal{M}) = \frac{1}{\sqrt{(2\pi)^{N_d} \sqrt{\det \mathbf{W}}}} \exp\left(-\frac{1}{2} \left[\boldsymbol{\mathcal{D}} - \mathbf{A}(\boldsymbol{\theta} | \mathcal{M}) \right]^T \mathbf{W}^{-1} \left[\boldsymbol{\mathcal{D}} - \mathbf{A}(\boldsymbol{\theta} | \mathcal{M}) \right] \right) \tag{29}$$

where N_d is the number of observations considered in the inverse analysis.

Although Eq. (27) completely defines the posterior distribution, its analytical evaluation is generally intractable. The Transitional Markov Chain Monte Carlo (TMCMC) method is therefore employed to generate posterior samples and estimate the model evidence. Originally proposed

by Ching and Chen [26], TMCMC has been applied and improved for Bayesian parameter estimation, model updating, and model class selection [23, 27].

For a given model class $\mathcal{M}_j$, TMCMC constructs a sequence of intermediate probability densities connecting the prior to the posterior,

$$p_k(\boldsymbol{\theta} \mid \boldsymbol{\mathcal{D}}, \mathcal{M}_j) \propto p(\boldsymbol{\mathcal{D}} \mid \boldsymbol{\theta}, \mathcal{M}_j)^{\beta_k} p(\boldsymbol{\theta} \mid \mathcal{M}_j), \qquad 0 = \beta_0 < \beta_1 < \cdots < \beta_K = 1. \tag{30}$$

At $\beta_0 = 0$, the intermediate density coincides with the prior, whereas at $\beta_K = 1$ it becomes the target posterior. Given N_s samples $\{\boldsymbol{\theta}_k^{(s)}\}_{s=1}^{N_s}$ distributed according to the density at stage k, the incremental importance weights are

$$w_k^{(s)} = p(\boldsymbol{\mathcal{D}} \mid \boldsymbol{\theta}_k^{(s)}, \mathcal{M}_j)^{\beta_{k+1} - \beta_k}. \tag{31}$$

The next tempering parameter β_{k+1} is selected adaptively by controlling the coefficient of variation of the weights. The weighted samples are then resampled and propagated through Metropolis–Hastings updates to generate the next intermediate population. This gradual transition improves the exploration of concentrated, correlated, or multimodal posterior distributions [26, 27]. As a byproduct of this sequence, the evidence is estimated as

$$p(\boldsymbol{\mathcal{D}} \mid \mathcal{M}_j) \approx \prod_{k=0}^{K-1} \left[\frac{1}{N_s} \sum_{s=1}^{N_s} w_k^{(s)} \right]. \tag{32}$$

3.2 Bayesian model class selection

Bayesian model class selection uses the evidence to compare the candidate classes in $\boldsymbol{\mathcal{M}}$ while accounting simultaneously for data-fitting capability and parameter-space complexity [41, 42]. According to Bayes' theorem, the posterior probability of model class $\mathcal{M}_j$ is

$$P(\mathcal{M}_j \mid \boldsymbol{\mathcal{D}}, \boldsymbol{\mathcal{M}}) = \frac{p(\boldsymbol{\mathcal{D}} \mid \mathcal{M}_j) P(\mathcal{M}_j \mid \boldsymbol{\mathcal{M}})}{\sum_{i=1}^{N_m} p(\boldsymbol{\mathcal{D}} \mid \mathcal{M}_i) P(\mathcal{M}_i \mid \boldsymbol{\mathcal{M}})}. \tag{33}$$

Here, $P(\mathcal{M}_j \mid \boldsymbol{\mathcal{M}})$ is the prior probability assigned to model class $\mathcal{M}_j$. In the present analysis, all candidate classes are considered equally plausible a priori, such that

$$P(\mathcal{M}_j \mid \boldsymbol{\mathcal{M}}) = \frac{1}{N_m}. \tag{34}$$

The model comparison is therefore governed exclusively by their evidences. From an information-theoretic perspective, the logarithm of the evidence can be decomposed as [23, 28, 42]

$$\ln p(\boldsymbol{\mathcal{D}} \mid \mathcal{M}_j) = \underbrace{\int_{\Theta_j} \ln[p(\boldsymbol{\mathcal{D}} \mid \boldsymbol{\theta}, \mathcal{M}_j)]\, p(\boldsymbol{\theta} \mid \boldsymbol{\mathcal{D}}, \mathcal{M}_j)\, \mathrm{d}\boldsymbol{\theta}}_{\text{posterior-averaged data fit}} - \underbrace{\int_{\Theta_j} \ln\left[\frac{p(\boldsymbol{\theta} \mid \boldsymbol{\mathcal{D}}, \mathcal{M}_j)}{p(\boldsymbol{\theta} \mid \mathcal{M}_j)}\right] p(\boldsymbol{\theta} \mid \boldsymbol{\mathcal{D}}, \mathcal{M}_j)\, \mathrm{d}\boldsymbol{\theta}}_{\text{information gain}}. \tag{35}$$

The first term is the posterior mean of the log-likelihood and measures the average agreement with the observations. The second term is the Kullback–Leibler divergence between the posterior and prior distributions and quantifies the information extracted from the data. It therefore penalizes models that require a strong contraction of their prior parameter space to reproduce the observations. Consequently, a more flexible constitutive model is favored only when its improvement in data agreement compensates for this additional information requirement. This built-in Occam effect enables model discrimination even when different calibrated models produce visually similar frequency-response curves.

Figure 3 provides a schematic overview of the proposed Bayesian identification and model-selection framework. The experimental acquisition stage illustrates the general application of the methodology; in the present numerical study, they are replaced by synthetic frequency-response observations generated with the finite-element reference model. For each candidate constitutive class, the GITT-based forward formulation is embedded in TMCMC to estimate the posterior parameter distribution and model evidence, which are subsequently used to calibrate, compare, and select the most plausible model.

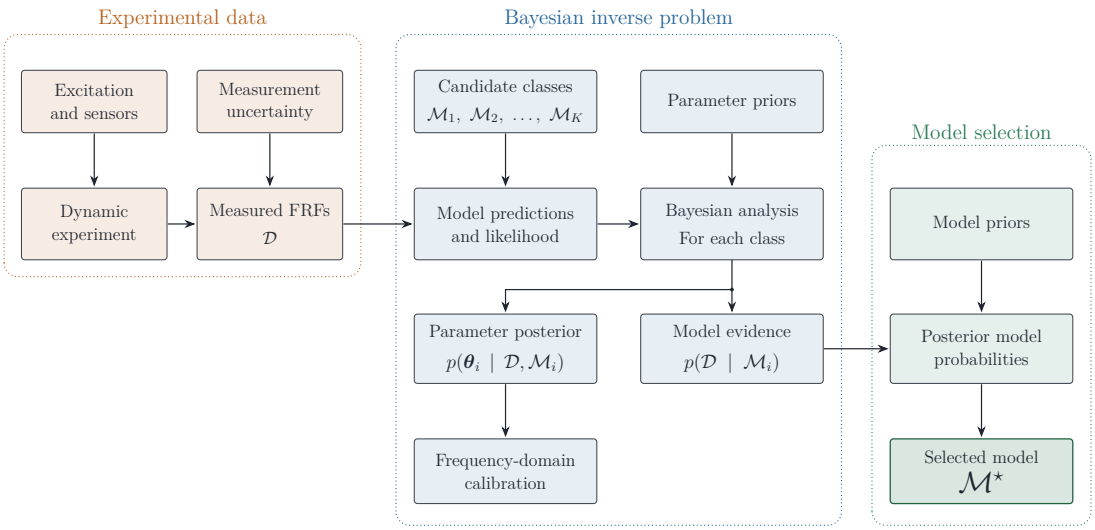


Figure 3: Schematic representation of the proposed Bayesian framework for constitutive-model identification and selection. The experimental branch illustrates how frequency-response data may be acquired from an instrumented beam. These observations are compared with GITT-based predictions from the candidate fractional viscoelastic models within TMCMC, providing posterior parameter distributions and model evidences for model calibration, Bayesian comparison, and selection.

4 Results and Discussion

The numerical results are organized in two main stages. First, the proposed forward model is verified against finite element results from literature for a two-layer viscoelastic cantilever beam, considering different viscoelastic-layer thicknesses. This step is necessary to assess whether the GITT-based formulation is able to reproduce the relevant dynamic behavior of the reference model before being used inside the Bayesian inverse framework. Then, the verified forward model is employed in the inverse analysis and in the Bayesian model class selection procedure, where different fractional viscoelastic constitutive laws are compared through their posterior distributions and model evidences.

4.1 Verification of the GITT solution (forward problem)

The proposed GITT-based formulation was verified against finite element results reported in the reference study by Cortés and Elejabarrieta [7]. In particular, the verification was performed for different thicknesses of the viscoelastic layer, since the relevance of shear-related effects increases as the damping layer becomes thicker.

Table 3 presents the physical and geometric parameters adopted in the reference problem. The system consists of a cantilever beam composed of a steel base layer and an unconstrained viscoelastic layer, subjected to a unitary harmonic force at the free end. The viscoelastic behavior is described by the four-parameter fractional model used in the reference study. For the GITT-based solution, the eigenfunction expansion was truncated at $N = 40$ modes, a value also adopted in the subsequent Bayesian inverse analyses.

Table 3: Physical and geometric parameters adopted from the reference study for the unconstrained viscoelastic two-layer cantilever beam. [7]

Category	**Parameter**	**Value**
Geometry	Beam length, L	$120\,\mathrm{mm}$
	Beam width, b	$10\,\mathrm{mm}$
	Base-layer thickness, H	$2\,\mathrm{mm}$
	Viscoelastic-layer thickness, H_1	$2,\ 6,\ 10\,\mathrm{mm}$
Base layer	Material	AISI T 316 L stainless steel
	Young's modulus, E	$176.2\,\mathrm{GPa}$
	Density, ρ	$7782\,\mathrm{kg/m^3}$
	Poisson's ratio, ν	0.3
Viscoelastic layer	Material	Soundown Vibration Damping Tile
	Density, ρ_1	$1423\,\mathrm{kg/m^3}$
	Poisson's ratio, ν_1	0.3
4P fractional model	E_0	$0.353\,\mathrm{GPa}$
	E_∞	$3.462\,\mathrm{GPa}$
	τ	$381.5\,\mu\mathrm{s}$
	α	0.873
Loading / configuration	Boundary condition	Cantilever beam
	External excitation	Unitary harmonic force at the free end

Figure 4 compares the frequency-response functions predicted by the GITT-based formulation with the finite element reference results for the different viscoelastic-layer thicknesses. The results show that the proposed formulation reproduces the reference response with very good agreement, including the resonance locations, amplitude levels, and overall decay trend. As expected, the discrepancies between the thin-layer approximation and the thick-layer response become more pronounced as the thickness of the viscoelastic layer increases. This behavior is consistent with the reference study, where shear deformation effects become increasingly relevant for thicker damping layers and higher frequencies [7].

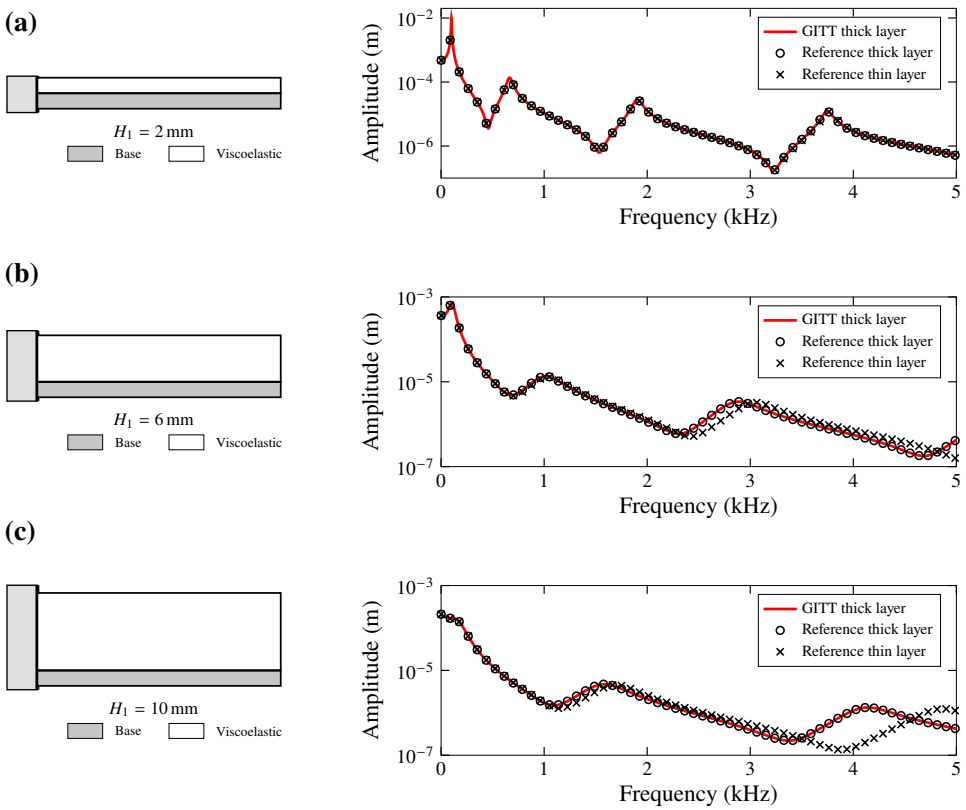


Figure 4: Numerical verification of the GITT-based formulation against finite element reference results presented in [7] for viscoelastic-layer thicknesses of (a) $H_1 = H$, (b) $H_1 = 3H$ and (c) $H_1 = 5H$. The thin-layer approach neglects the shear effects of the viscoelastic layer, whereas the thick-layer approach accounts for these effects.

The agreement observed in Fig. 4 supports the use of the GITT formulation as the forward model in the subsequent inverse analysis. The Generalized Integral Transform Technique provides a hybrid analytical–numerical formulation in which the spatial dependence is represented through an eigenfunction expansion rather than by a conventional spatial discretization. This leads to a compact reduced-order description of the beam dynamics while preserving the main mechanical features associated with the layered viscoelastic structure. In the present context, this characteristic is particularly useful because the TMCMC algorithm requires a large number of forward model evaluations.

In addition, the verification strategy adopted here helps to mitigate the so-called inverse crime. The synthetic data used in the identification procedure are generated from the finite element model taken from the reference solution, whereas the inversion itself is performed using a different forward formulation based on GITT. Therefore, the data-generating model and the inversion model are not identical, which makes the identification problem more realistic and avoids an

artificially favorable assessment of the Bayesian framework.

4.2 Bayesian model class selection results

The thin- and thick-layer configurations were analyzed within the same probabilistic framework to determine how the layer thickness affects parameter identifiability and model discrimination. Synthetic observations were generated with the finite-element model using the experimentally calibrated parameters reported by Cortés and Elejabarrieta [7], listed in Table 4.

Table 4: Fractional Zener model parameters adopted as reference values for generating the synthetic observations [7].

Parameter	Symbol	Value
Equilibrium modulus	E_0	0.353 GPa
Instantaneous modulus	E_∞	3.462 GPa
Relaxation time	τ	381.5 μs
Fractional order	α	0.873

The vector of synthetic observed data $\boldsymbol{\mathcal{D}}$ was obtained by adding Gaussian noise to the base-10 logarithm of the reference frequency-response amplitudes, according to

$$\boldsymbol{\mathcal{D}} = \log_{10}(\boldsymbol{Y_r}) + \boldsymbol{\varepsilon_\ell}, \qquad \boldsymbol{\varepsilon_\ell} \sim \mathcal{N}(\boldsymbol{0}, \boldsymbol{W}), \tag{36}$$

where $\boldsymbol{Y_r}$ is the vector of the corresponding amplitudes provided by the finite-element reference model, and $\boldsymbol{\varepsilon_\ell}$ is a vector of observation errors, assumed to follow a multivariate Gaussian distribution with zero mean and covariance matrix $\boldsymbol{W} = \sigma_e^2 \boldsymbol{I}$, where σ_e^2 is the noise variance and $\boldsymbol{I}$ is the identity matrix. In this study, the noise standard deviation was set to $\sigma_e = 0.05$ in the base-10 logarithmic amplitude domain, corresponding to multiplicative lognormal noise in the original amplitude scale. The same logarithmic transformation was applied to the model predictions when evaluating the likelihood function.

The same synthetic data realization was used for all candidate models. Fractional Kelvin–Voigt, Maxwell, and Zener models were compared under the broad uniform priors summarized in Table 5. Ten independent TMCMC runs were performed for each model and layer configuration. For the Bayesian inverse analysis, two configurations were considered: a thin viscoelastic layer with $H_1 = 2$ mm and a thick viscoelastic layer with $H_1 = 10$ mm, both with a base-layer thickness of $H = 2$ mm. The synthetic observations were generated at 140 uniformly spaced frequencies between 1 and 5000 Hz. The numerical simulations were conducted using TMCMC with $N_s = 5000$ samples per transitional stage, a single Metropolis–Hastings step, and a target coefficient of variation for the importance weights of $\nu_{\mathrm{CoV}} = 100\%$.

Variance-based global sensitivity analysis (GSA) quantifies how the uncertainty in the model

Table 5: Prior distributions adopted for the uncertain parameters of each candidate constitutive model.

Model	Parameter	Prior distribution	Unit
Fractional Kelvin–Voigt	E	$\mathcal{U}(0.001, 10)$	GPa
	η	$\mathcal{U}(10^{-8}, 10^{2})$	$\mathrm{GPa\,s}^{\alpha}$
	α	$\mathcal{U}(0.05, 0.99)$	–
Fractional Maxwell	E	$\mathcal{U}(0.001, 20)$	GPa
	η	$\mathcal{U}(10^{-8}, 10^{2})$	$\mathrm{GPa\,s}^{\alpha}$
	α	$\mathcal{U}(0.05, 0.99)$	–
Fractional Zener	E_0	$\mathcal{U}(0.001, 5)$	GPa
	E_∞	$\mathcal{U}(0.001, 20)$	GPa
	τ	$\mathcal{U}(10^{-8}, 10^{2})$	s
	α	$\mathcal{U}(0.05, 0.99)$	–

inputs contributes to the variability of a prescribed quantity of interest over the complete admissible parameter domain. Unlike local methods, it can capture nonlinear effects and interactions among parameters. Sobol indices provide a variance decomposition in which the first-order index, S_1, measures the direct contribution of a parameter, the total-order index, S_T, includes its direct contribution and all interactions with the remaining parameters, and the second-order index, S_2, quantifies pairwise interactions. Further details on variance-based GSA and Sobol indices can be found in [32, 33].

In the present analysis, the quantity of interest is the log-likelihood function rather than the response amplitude at a particular frequency. Consequently, the indices quantify how each constitutive parameter and parameter interaction affects the agreement between the predicted and observed responses over the prior domain. This likelihood-based formulation provides a preliminary diagnostic of parameter identifiability: parameters with negligible sensitivity are expected to remain weakly informed by the data, whereas strong interaction effects may indicate compensation and posterior correlation. Nevertheless, the Sobol indices do not directly determine posterior identifiability, which also depends on the observation noise, prior distributions, frequency range, and local geometry of the likelihood. Their diagnostic capability is therefore assessed subsequently through the posterior distributions and repeated-run statistics. Figure 5 presents the resulting indices for both layer configurations and all candidate models.

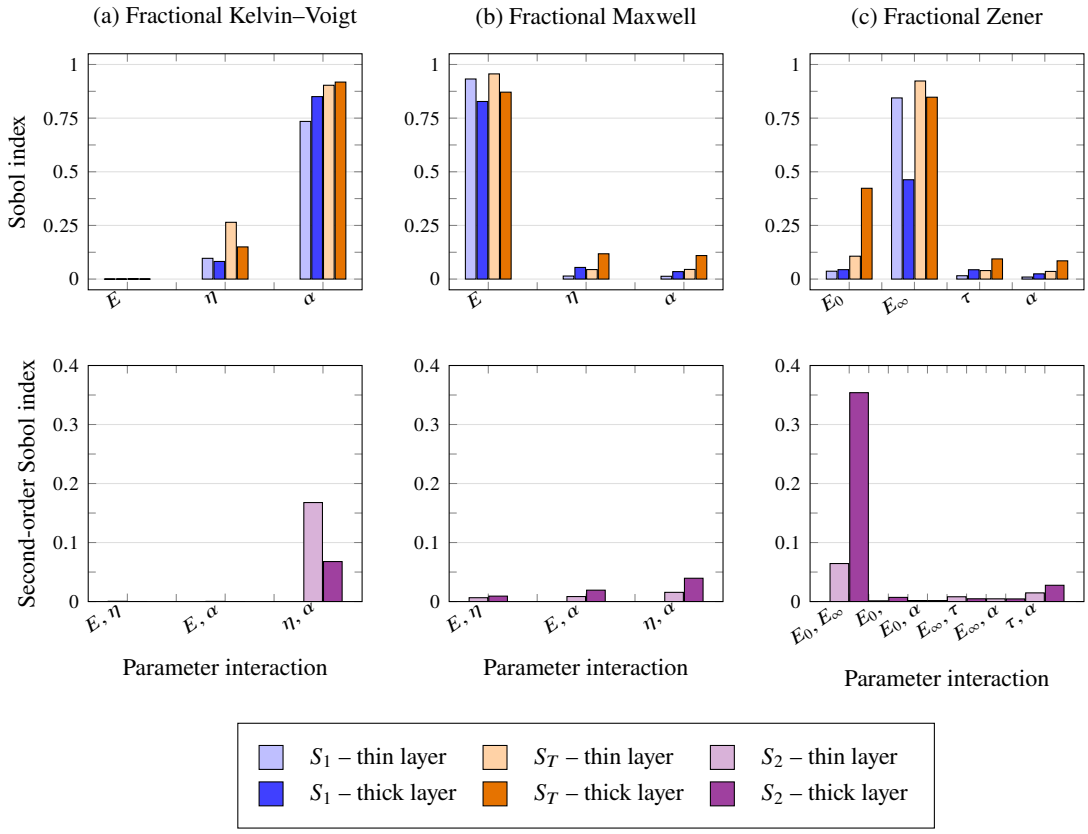


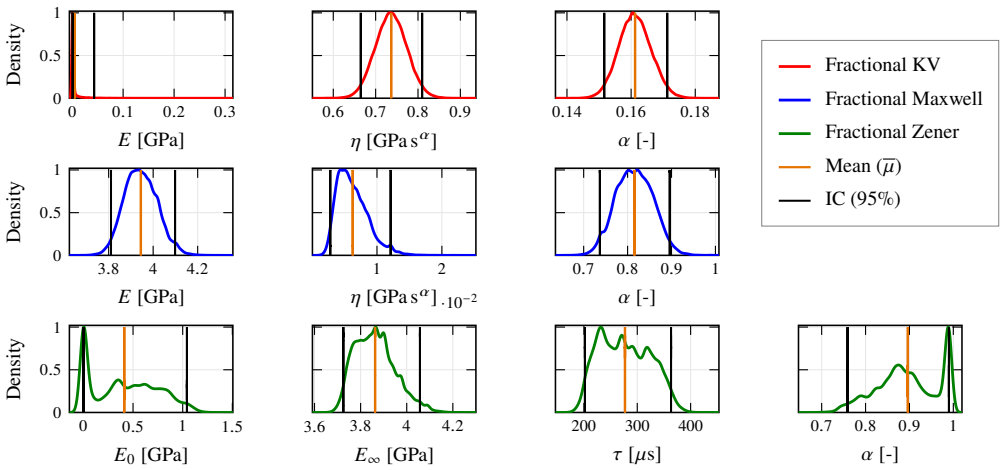
Figure 5: Comparative analysis between first-order (S_1), total-effect (S_T), and second-order (S_2) Sobol indices for the thin and thick viscoelastic layers: (a) fractional Kelvin–Voigt, (b) fractional Maxwell, and (c) fractional Zener models.

The dominant sensitivity directions are primarily determined by the constitutive model. In the Kelvin–Voigt model, α controls most of the likelihood variation for both thicknesses, E is practically inactive, and the main interaction occurs between η and α. This interaction is more pronounced for the thin layer, but the overall ranking is unchanged. In the Maxwell model, E dominates both S_1 and S_T, while η, α, and their interactions have comparatively small contributions.

The Zener model exhibits the strongest thickness dependence. For the thin layer, E_∞ provides most of the first-order contribution, whereas E_0 has only a limited independent effect. Increasing the layer thickness substantially increases the total effect of E_0 and, more importantly, the E_0–E_∞ interaction. The thick configuration activates a coupled stiffness contribution that is weakly expressed in the thin-layer response. This behavior follows from the additional mechanical pathway through which the complex modulus affects the shear modulus, equivalent stiffness, bending rigidity, and ultimately the measured frequency response.

The posterior densities in Figure 6 provide a complementary assessment of practical identifiability. For Kelvin–Voigt, the modulus E remains weakly informed in both configurations, consistently with its negligible Sobol index. Although η and α exhibit concentrated posteriors, this concentration does not compensate for the model's inability to reproduce the data.

(a) Thin-layer case



(b) Thick-layer case

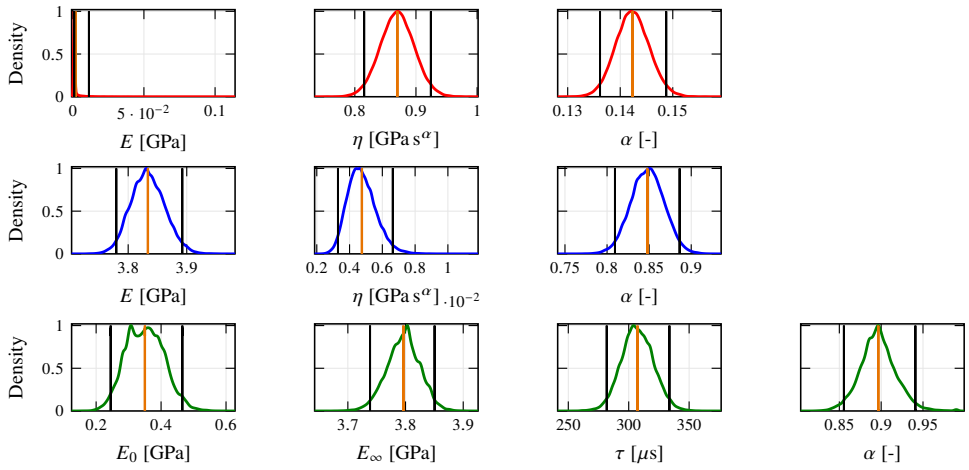


Figure 6: Marginal posterior densities for the candidate constitutive models in the (a) thin- and (b) thick-layer configurations. Orange lines indicate posterior means, and black lines delimit the corresponding 95% credible intervals.

Table 6 complements the marginal posterior densities by quantifying the repeatability of the estimates over the ten independent TMCMC runs. Here, $\overline{\mu}$ is the mean of the run-specific posterior means, $\mathrm{sd}_{\mathrm{run}}(\mu)$ is their between-run standard deviation, $\mathrm{CV}_{\mathrm{run}}(\mu)$ is the corresponding coefficient of variation, and the last column reports the mean width of the 95% credible interval.

Table 6: Posterior summary for the thin- and thick-layer configurations.

Model	Parameter	$\overline{\mu}$	$\mathrm{sd}_{\mathrm{run}}(\mu)$	$\mathrm{CV}_{\mathrm{run}}(\mu)$ (%)	Mean 95% CrI width
Thin-layer configuration					
Kelvin–Voigt	E (GPa)	0.0048	0.0007	13.88	0.0425
	η (GPas$^{\alpha}$)	0.7366	0.0008	0.11	0.1448
	α	0.1612	0.0001	0.06	0.0196
Maxwell	E (GPa)	3.9450	0.0211	0.53	0.2773
	η (GPas$^{\alpha}$)	0.0063	0.0007	12.21	0.0085
	α	0.8156	0.0136	1.67	0.1527
Zener	E_0 (GPa)	0.4114	0.2042	49.63	0.8755
	E_∞ (GPa)	3.8627	0.2439	7.07	1.0560
	τ (μs)	277.0021	29.5440	10.67	133.2308
	α	0.8964	0.0394	4.39	0.1849
Thick-layer configuration					
Kelvin–Voigt	E (GPa)	0.0019	0.0001	7.33	0.0106
	η (GPas$^{\alpha}$)	0.8693	0.0007	0.08	0.1117
	α	0.1424	0.0001	0.05	0.0129
Maxwell	E (GPa)	3.8337	0.0032	0.08	0.1115
	η (GPas$^{\alpha}$)	0.0047	0.0001	2.69	0.0033
	α	0.8480	0.0029	0.35	0.0760
Zener	E_0 (GPa)	0.3503	0.0193	5.52	0.2081
	E_∞ (GPa)	3.7963	0.0245	0.71	0.2487
	τ (μs)	307.2920	4.1315	1.34	49.5660
	α	0.8966	0.0078	0.87	0.0770

Table 6 quantitatively complements the marginal posterior distributions by distinguishing between repeated-run stability and posterior uncertainty. Lower values of $\mathrm{CV}_{\mathrm{run}}(\mu)$ indicate greater consistency across independent TMCMC runs, whereas narrower credible intervals provide more direct evidence of improved practical identifiability. Both measures are systematically lower for the thick-layer configuration. The improvement is particularly pronounced for the Zener model, for which the coefficients of variation of E_0 and τ decrease from approximately 50% and 10% to 5.52% and 1.34%, respectively, while all credible intervals become narrower. Similar, although less pronounced, improvements are observed for the Maxwell and Kelvin–Voigt models.

The model-specific posterior patterns agree with the likelihood-based sensitivity analysis. For the thin layer, the Maxwell modulus and fractional order are comparatively well constrained, whereas η remains more uncertain. In contrast, the weak direct contributions of E_0 and τ in the Zener model, together with parameter compensation, result in broad marginal distributions and greater run-to-run variability. Likewise, the negligible sensitivity of the Kelvin–Voigt modulus is reflected in its weak posterior contraction.

For the thick layer, the greater overall sensitivity of the likelihood to the constitutive parameters is accompanied by reduced posterior ambiguity, particularly for the Zener model, although the Maxwell posteriors also become more concentrated. Overall, the agreement between the sensitivity measures and the posterior results shows that likelihood-based GSA can anticipate weak or coupled parameter directions before the complete Bayesian analysis, although it does not replace the posterior assessment of practical identifiability.

Within the Maxwell and Zener models, the increase in layer thickness affects posterior concentration much more strongly than posterior location. The mean parameter estimates remain broadly consistent across the two configurations, with the differences generally being small relative to the posterior uncertainty of the thin-layer case. This consistency is physically meaningful because the intrinsic constitutive properties should not change solely as a consequence of layer thickness.

The two configurations therefore indicate similar constitutive parameter regions, but with markedly different levels of epistemic resolution. The thin-layer response admits a broad set of compensating parameter combinations, whereas the thick-layer response preserves approximately the same central estimates while substantially reducing the admissible parameter region.

The orange vertical lines in Figure 6 define the posterior mean of each parameter. For each candidate model and layer configuration, these posterior means were assembled into a parameter vector and substituted into the corresponding constitutive relation. The resulting parameter vectors were then used to evaluate the deterministic frequency-response curves shown in panels (a) and (b) of Figure 7.

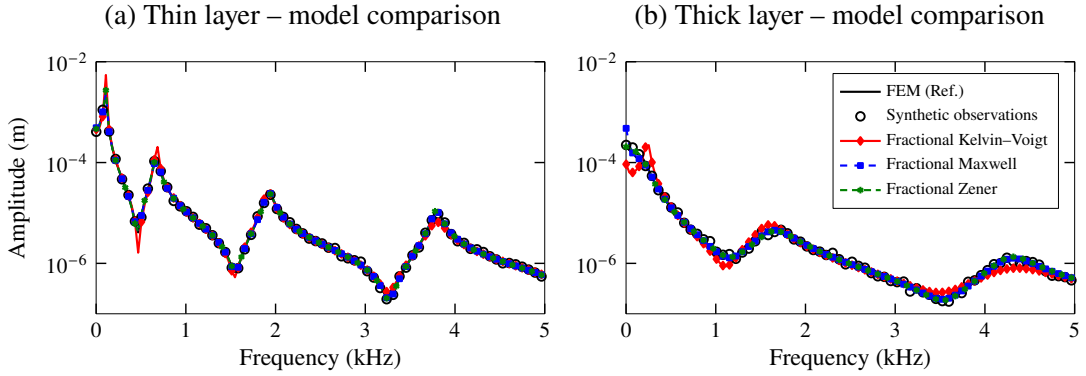


Figure 7: Frequency responses evaluated at the posterior-mean parameter estimates for the candidate models in the (a) thin- and (b) thick-layer configurations.

For the thin layer, the posterior-mean Maxwell and Zener responses both reproduce the principal resonances and antiresonances, whereas Kelvin–Voigt shows systematic discrepancies, particularly near the sharp low-frequency features. Maxwell and Zener are therefore difficult to distinguish by the data fit agreement alone. Similar behavior is observed for the thick-layer

case.

Bayesian evidence resolves this ambiguity by balancing posterior-averaged data agreement against the information required to constrain the parameters. Unlike comparisons based solely on calibrated responses, it determines whether an improvement in fit is sufficient to justify additional constitutive complexity. Table 7 summarizes this balance over the ten independent TMCMC runs. The data-fit term is the posterior-averaged log-likelihood and measures agreement with the observations, whereas the information gain is the Kullback–Leibler divergence from the prior to the posterior and represents the amount of parameter restriction required by the data. The log-evidence combines these contributions, with larger values indicating stronger model support. The SD measures variability between TMCMC runs, while the mean model probability expresses the relative support for each candidate model.

Table 7: Bayesian model-selection results, averaged over the ten independent TMCMC runs, for the thin and thick-layer configurations.

Configuration	Model	Mean data fit	Mean information gain	Mean log-evidence	SD log-evidence	Mean model probability (%)
Thin	Fractional Kelvin–Voigt	-183.14	14.23	-197.38	0.51	≈ 0
	Fractional Maxwell	-64.71	15.05	$\mathbf{-79.76}$	0.78	$\mathbf{87.75}$
	Fractional Zener	-63.81	17.92	-81.73	0.98	12.25
Thick	Fractional Kelvin–Voigt	-493.8	14.87	-508.67	4.33	≈ 0
	Fractional Maxwell	-102.29	18.52	-120.81	0.69	≈ 0
	Fractional Zener	-66.50	23.73	$\mathbf{-90.23}$	2.09	$\mathbf{100.00}$

For the thin layer, Maxwell is consistently selected even though Zener provides a closer representation of the reference response. Because the viscoelastic layer contributes only weakly to the global dynamics, the additional Zener mechanisms are not sufficiently expressed in the observations. Their modest improvement in data agreement therefore does not compensate for the greater information required to constrain the additional parameter combinations. Maxwell consequently emerges as the most parsimonious effective description, illustrating the Bayesian form of Occam's razor.

For the thick layer, the greater mechanical participation of the viscoelastic material makes the differences among the constitutive models more observable. The improvement provided by Zener then clearly outweighs its additional information cost, resulting in a posterior model probability close to unity and a first-place ranking in every run. The rejection of Kelvin–Voigt in both configurations further shows that Bayesian evidence does not favor simplicity unconditionally, but only when predictive adequacy is preserved. The thin layer masks part of the material behavior and supports Maxwell as an effective model, whereas the thick layer exposes sufficient information to justify Zener. Together with the sensitivity and posterior analyses, the evidence therefore connects parameter influence, practical identifiability, and data-supported model complexity.

This result also has an important experimental-design implication: structural geometry controls

how strongly the constitutive behavior is expressed in the measured response and, consequently, how much information is available to the inverse analysis. Within the configurations investigated here, the thicker layer improves practical identifiability and reveals constitutive features that remain weakly observable in the thin layer, although the associated parameter interactions must still be considered. Finally, the reported posterior model probabilities are conditional on the candidate set, prior ranges, noise model, and frequency interval adopted in this study.

Following model selection, posterior uncertainty was propagated through the evidence-supported models to assess their predictive adequacy beyond point estimates. Figure 8 presents the posterior predictive medians and corresponding 95% intervals for the Maxwell model selected in the thin-layer case and the Zener model selected in the thick-layer case. These intervals show the range of responses supported by the posterior uncertainty and indicate whether the selected models consistently reproduce the observed structural behavior.

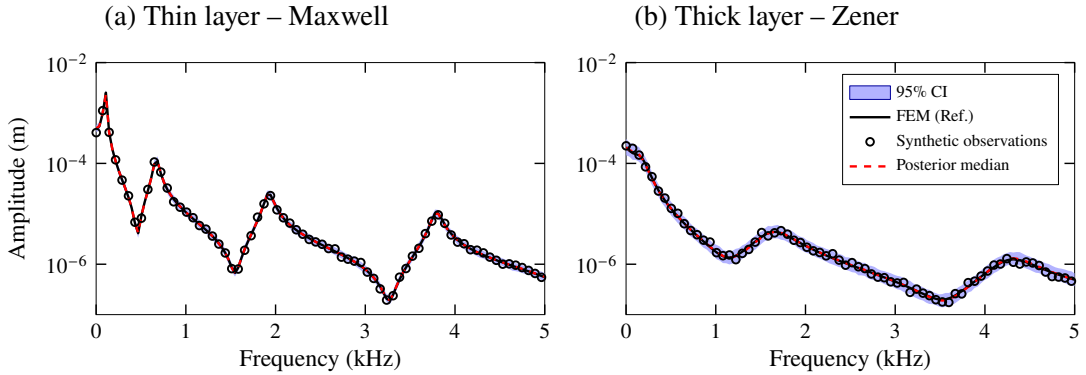


Figure 8: Posterior predictive medians and credible intervals. (a) Maxwell model selected in the thin layer configuration. (b) Zener model selected in the thick layer configuration.

5 Concluding Remarks

This work presented a Bayesian framework for parameter inference and model class selection of fractional viscoelastic constitutive laws in cantilever beams with unconstrained damping layers. The structural response was formulated in the frequency domain using a unified representation for thin layers and shear-corrected thick layers, while a GITT-based solution was adopted as the forward model in the inverse analysis.

The GITT predictions showed very good agreement with the finite element reference solutions in terms of resonance locations, amplitudes, and the overall frequency-response behavior. This agreement supports the use of the semi-analytical formulation in Bayesian analyses requiring repeated forward evaluations. Moreover, generating the synthetic observations with an independently implemented finite element model while performing the inversion with the GITT formu-

lation helped to mitigate the inverse-crime effect.

The synthetic observations were generated using a four-parameter fractional reference law whose parameters were obtained from the experimental characterization reported by Cortés and Elejabarrieta [34]. The reference law was used exclusively for data generation, whereas the Bayesian comparison considered the fractional Kelvin–Voigt, Maxwell, and Zener models.

The likelihood-based global sensitivity analysis provided useful information about how the constitutive parameters affect the agreement between the predicted and observed responses. The differences between the first- and total-order Sobol indices revealed relevant parameter interactions, which were subsequently reflected in posterior correlations, broad marginal distributions, and run-to-run variability. These results show that sensitivity analysis can provide valuable diagnostics for interpreting the conditioning of the inverse problem. Nevertheless, the Sobol indices should not be regarded as direct measures of posterior identifiability, which also depends on the observation noise, prior distributions, frequency range, and compensating effects among parameters.

For the thin-layer configuration, the fractional Maxwell model achieved the largest mean Bayesian evidence and was ranked first in all independent TMCMC runs. The Zener model remained a competitive alternative, whereas the fractional Kelvin–Voigt model received negligible posterior support. When transverse shear is negligible, the structural response does not contain sufficient discriminatory information to support the complete bounded relaxation behavior represented by the Zener parameterization. Under these conditions, the Maxwell model provides the most plausible effective description within the candidate set.

A different result was obtained for the thick-layer configuration, for which the fractional Zener model was decisively favored and ranked first in all TMCMC runs. The thick-layer FRF carries more information about the frequency-dependent transition between the low- and high-frequency material moduli. Since the Zener model is mathematically equivalent to the reference constitutive class under an appropriate parameter transformation, its selection in the thick-layer case can be interpreted as recovery of the data-generating constitutive family.

The contrast between the two configurations constitutes the main result of the study. The underlying reference material was unchanged, but the Bayesian analysis favored different constitutive representations because the mechanical configuration changed the amount and type of information transmitted from the material behavior to the measured FRF. Thus, constitutive-model selection from structural measurements depends not only on the material law, but also on the geometry and deformation mechanisms of the test specimen.

The posterior and sensitivity results further showed that transverse shear changes the inverse mapping between structural observations and constitutive parameters. The thick-layer configuration generally produced stronger posterior contraction and greater model-discrimination capability, indicating that specimen geometry should be considered part of the experimental-design problem. Configurations that activate multiple deformation mechanisms may provide more informative measurements for identifying frequency-dependent material properties.

The conclusions remain conditional on the candidate-model set, prior domains, observation-noise assumptions, and analyzed frequency range. Moreover, the present study was based on synthetic observations, although the reference constitutive parameters were experimentally grounded. Future work should therefore apply the framework to measured FRFs, investigate the sensitivity of the evidence to alternative prior specifications, incorporate additional sources of experimental and structural-model uncertainty, and consider Bayesian model averaging when no single constitutive class receives decisive posterior support.

Declaration of interests

The authors declare that they have no known competing financial interests or personal relationships that could have appeared to influence the work reported in this paper.

Data availability

Data will be made available on request.

Author contributions

L.S.A: Conceptualization, Data curation, Methodology, Visualization, Formal analysis, Writing – original draft and review. A.J.P.O: Visualization, Formal analysis, Writing – original draft and review. A.A: Conceptualization, Methodology, Supervision, Visualization, Formal analysis, Writing – original draft. D.C.K: Conceptualization, Methodology, Supervision, Visualization, Project administration, Supervision, Writing – review and editing. L.T.S: Conceptualization, Methodology, Visualization, Project administration, Supervision, Writing – review and editing.

Funding information

This study was financed in part by the Coordenação de Aperfeiçoamento de Pessoal de Nível Superior - Brasil (CAPES) Finance Code 001 and FAPERJ - Fundação Carlos Chagas Filho de Amparo à Pesquisa do Estado do Rio de Janeiro.

Acknowledgements

The authors also thank Polytechnic Institute, Rio de Janeiro State University, IPRJ/UERJ, Brazil and Federal Institute of Northern Minas Gerais, IFNMG, Brazil.

References

[1] A. D. Nashif, D. I. G. Jones, and J. P. Henderson, Vibration Damping. New York: John Wiley & Sons, 1985.

[2] D. I. G. Jones, Handbook of Viscoelastic Vibration Damping. Chichester: John Wiley & Sons, 2001.

[3] H. Oberst and K. Frankenfeld, "Über die dämpfung der biegeschwingungen dünner bleche durch fest haftende beläge," Acustica, vol. 2, pp. 181–194, 1952.

[4] D. Ross, E. M. Kerwin, and E. E. Ungar, "Damping of plate flexural vibrations by means of viscoelastic laminae," in Structural Damping, pp. 49–88, New York: American Society of Mechanical Engineers, 1959.

[5] S.-Y. Kim and D.-H. Lee, "Identification of fractional-derivative-model parameters of viscoelastic materials from measured FRFs," Journal of Sound and Vibration, vol. 324, no. 3–5, pp. 570–586, 2009.

[6] W. Sun, Z. Wang, R. Liu, and X. Yan, "Inverse identification of the frequency-dependent mechanical parameters of a viscoelastic core layer based on the vibration response," Applied Sciences, vol. 7, no. 5, p. 455, 2017.

[7] F. Cortés and M. J. Elejabarrieta, "Structural vibration of flexural beams with thick unconstrained layer damping," International Journal of Solids and Structures, vol. 45, no. 22-23, pp. 5805–5813, 2008.

[8] F. Cortés and M. J. Elejabarrieta, "Homogenised finite element for transient dynamic analysis of unconstrained layer damping beams involving fractional derivative models," Computational Mechanics, vol. 40, pp. 313–324, 2007.

[9] M. Brun, F. Cortés, and M. J. Elejabarrieta, "Transient dynamic analysis of unconstrained layer damping beams characterized by a fractional derivative model," Mathematics, vol. 9, no. 15, p. 1731, 2021.

[10] D. F. Golla and P. C. Hughes, "Dynamics of viscoelastic structures: A time-domain, finite element formulation," Journal of Applied Mechanics, vol. 52, no. 4, pp. 897–906, 1985.

[11] D. J. McTavish and P. C. Hughes, "Modeling of linear viscoelastic space structures," Journal of Vibration and Acoustics, vol. 115, no. 1, pp. 103–110, 1993.

[12] A. Schmidt and L. Gaul, "Finite element formulation of viscoelastic constitutive equations using fractional time derivatives," Nonlinear Dynamics, vol. 29, pp. 37–55, 2002.

[13] R. L. Bagley and P. J. Torvik, "A theoretical basis for the application of fractional calculus to viscoelasticity," Journal of Rheology, vol. 27, no. 3, pp. 201–210, 1983.

[14] R. L. Bagley and P. J. Torvik, "On the fractional calculus model of viscoelastic behavior," Journal of Rheology, vol. 30, no. 1, pp. 133–155, 1986.

[15] F. Mainardi, Fractional Calculus and Waves in Linear Viscoelasticity: An Introduction to Mathematical Models. London: Imperial College Press, 2010.

[16] Y. A. Rossikhin and M. V. Shitikova, "Application of fractional calculus for dynamic problems of solid mechanics: Novel trends and recent results," Applied Mechanics Reviews, vol. 63, no. 1, p. 010801, 2010.

[17] M. Martinez-Agirre and M. J. Elejabarrieta, "Dynamic characterization of high damping viscoelastic materials from vibration test data," Journal of Sound and Vibration, vol. 330, no. 16, pp. 3930–3943, 2011.

[18] M. Klanner, M. S. Prem, and K. Ellermann, "Steady-state harmonic vibrations of viscoelastic timoshenko beams with fractional derivative damping models," Applied Mechanics, vol. 2, no. 4, pp. 797–819, 2021.

[19] J. Calaf-Chica, V. Cea-González, M.-J. García-Tárrago, and F.-J. Gómez-Gil, "Fractional viscoelastic models for the estimation of the frequency response of rubber bushings based on relaxation tests," Results in Engineering, vol. 20, p. 101465, 2023.

[20] E. Barkanov, E. Skukis, and B. Petitjean, "Characterisation of viscoelastic layers in sandwich panels via an inverse technique," Journal of Sound and Vibration, vol. 327, no. 3–5, pp. 407–412, 2009.

[21] J. L. Beck and K.-V. Yuen, "Model selection using response measurements: Bayesian probabilistic approach," Journal of Engineering Mechanics, vol. 130, no. 2, pp. 192–203, 2004.

[22] D. J. C. MacKay, Information Theory, Inference, and Learning Algorithms. Cambridge: Cambridge University Press, 2003.

[23] M. Muto and J. L. Beck, "Bayesian updating and model class selection for hysteretic structural models using stochastic simulation," Journal of Vibration and Control, vol. 14, no. 1–2, pp. 7–34, 2008.

[24] J. Kaipio and E. Somersalo, Statistical and Computational Inverse Problems, vol. 160 of Applied Mathematical Sciences. New York: Springer, 2005.

[25] A. Gelman, J. B. Carlin, H. S. Stern, D. B. Dunson, A. Vehtari, and D. B. Rubin, Bayesian Data Analysis. Boca Raton: CRC Press, 3 ed., 2013.

[26] J. Ching and Y.-C. Chen, "Transitional markov chain monte carlo method for bayesian model updating, model class selection, and model averaging," Journal of Engineering Mechanics, vol. 133, no. 7, pp. 816–832, 2007.

[27] W. Betz, I. Papaioannou, and D. Straub, "Transitional markov chain monte carlo: Observations and improvements," Journal of Engineering Mechanics, vol. 142, no. 5, p. 04016016, 2016.

[28] L. S. Asth, D. C. Knupp, L. T. Stutz, L. A. Abreu, and B. C. Lugão, "Bayesian parameter estimation and model class selection for identification of spatially dependent convective heat transfer coefficients in a microtube heat sink," International Journal of Applied and Computational Mathematics, vol. 12, no. 5, p. 70, 2026.

[29] R. M. Cotta and M. D. Mikhailov, "The integral transform method," Applied Mathematical Modelling, vol. 17, no. 3, pp. 156–161, 1993.

[30] R. M. Cotta, Integral Transforms in Computational Heat and Fluid Flow. Boca Raton: CRC Press, 1993.

[31] C. F. T. Matt, "Combined classical and generalized integral transform approaches for the analysis of the dynamic behavior of a damaged structure," Applied Mathematical Modelling, vol. 37, no. 18–19, pp. 8431–8450, 2013.

[32] I. M. Sobol', "Global sensitivity indices for nonlinear mathematical models and their monte carlo estimates," Mathematics and Computers in Simulation, vol. 55, no. 1–3, pp. 271–280, 2001.

[33] A. Saltelli, M. Ratto, T. Andres, F. Campolongo, J. Cariboni, D. Gatelli, M. Saisana, and S. Tarantola, Global Sensitivity Analysis: The Primer. Chichester: John Wiley & Sons, 2008.

[34] F. Cortés and M. Elejabarrieta, "Viscoelastic materials characterisation using the seismic response," Materials & Design, vol. 28, no. 7, pp. 2054–2062, 2007.

[35] R. M. Cotta and M. D. Mikhailov, Heat Conduction: Lumped Analysis, Integral Transforms, Symbolic Computation. Chichester: Wiley-Interscience, 1997.

[36] L. Meirovitch, Elements of Vibration Analysis. McGraw-Hill, 2nd ed., 1986.

[37] S. S. Rao, Mechanical Vibrations. Prentice Hall, 5th ed., 2011.

[38] R. M. Cotta, D. C. Knupp, and C. P. Naveira-Cotta, Analytical Heat and Fluid Flow in Microchannels and Microsystems. Springer International Publishing, 2016.

[39] L. S. Katafygiotis, C. Papadimitriou, and H. F. Lam, "A probabilistic approach to structural model updating," Soil Dynamics and Earthquake Engineering, vol. 17, pp. 495–507, 1998.

[40] J. P. Kaipio and C. Fox, "The bayesian framework for inverse problems in heat transfer," Heat Transfer Engineering, vol. 32, no. 9, pp. 718–753, 2011.

[41] S. H. Cheung and J. L. Beck, "Calculation of posterior probabilities for bayesian model class assessment and averaging from posterior samples based on dynamic system data," Computer-Aided Civil and Infrastructure Engineering, vol. 25, pp. 304–321, 2010.

[42] K. H. Knuth, M. Habeck, N. K. Malakar, A. M. Mubeen, and B. Placek, "Bayesian evidence and model selection," Digital Signal Processing, vol. 47, pp. 50–67, 2015.